

## **NaI and CaII absorption components observed towards the Orion-Eridanus Superbubble<sup>★</sup>**

B. Y. Welsh<sup>1</sup>, S. Sallmen<sup>2</sup>, and S. Jelinsky<sup>1</sup>

<sup>1</sup> Experimental Astrophysics Group, Space Sciences Laboratory, UC Berkeley, Berkeley, CA 94720, USA  
e-mail: bwelsh@ssl.berkeley.edu

<sup>2</sup> Department of Physics, Univ. of Wisconsin – La Crosse, La Crosse, WI 54601, USA

Received 13 January 2005 / Accepted 19 May 2005

**Abstract.** We present medium-resolution spectra ( $R \sim 7.5 \text{ km s}^{-1}$ ) of the interstellar NaI and CaII interstellar absorption lines observed towards 16 early-type stars with distances of 160–1 kpc in the line-of-sight towards the Orion-Eridanus Superbubble (OE-S). These data have been supplemented with measurements of NaI absorption towards a further 13 stars with similar sight-lines taken from the literature. We detect two major absorption components with velocities of  $V_{\text{lsr}} \sim +7.0$  and  $-8.0 \text{ km s}^{-1}$ . The former component, seen in 70% of the sight-lines is associated with the boundary to the Local Bubble cavity located at a distance of 140–150 pc. The other absorption component is only detected towards a limited region of the sky bounded by ( $190^\circ < l < 215^\circ$ ) and ( $-50^\circ < b < -30^\circ$ ). If gas with this velocity is associated with an outer expansion shell of the OE-S, then we can place its distance at 163–180 pc in agreement with the estimate by Guo et al. (1995, ApJ, 453, 256). Several other negative velocity components at  $V_{\text{lsr}} \sim -20.4, -28.5$  and  $-33.5 \text{ km s}^{-1}$  have also been detected for sight-line distances  $> 220$  pc within an area coincident with that of the 0.75 keV X-ray enhancement of the OE-S. Column density ratios,  $N(\text{NaI})/N(\text{CaII})$ , for the most negative velocity components have values  $< 1.0$ , suggesting that this gas has been disrupted by a possible shock event. Our data do not support a simple model for the OE-S that involves a single stellar bubble cavity that stretches from the Orion Nebula to high galactic latitudes. Instead, our detection of multiple positive and negative velocity components suggests the presence of several gas shells produced by supernovae and/or stellar wind-driven shocks. We also confirm that the prominent “hook-like” feature of H- $\alpha$  emission that characterizes the OE-S, in fact composed of two physically separate emission arcs, with the brighter Arc A being at a distance  $> 500$  pc. Finally, we place a similar distance limit for any coherently structured rear shell of neutral gas associated with expansion of the OE-S towards the galactic halo.

**Key words.** ISM: bubbles – ISM: kinematics and dynamics

### **1. Introduction**

Recent 3-D maps of the neutral absorption characteristics of gas surrounding the Sun to within 250 pc have revealed several narrow “interstellar tunnels” that connect the Local Bubble to several adjacent similarly rarefied interstellar cavities (Lallement et al. 2003). This picture is similar to the model of the general interstellar medium (ISM) first forwarded by Cox & Smith (1974) in which the large-scale effect of the expansion of supernova remnants (and stellar winds) within the ISM is to generate a system of rarefied “bubbles” interconnected by very low-density gas tunnels. One of these nearby cavities is the Orion-Eridanus superbubble (hereafter, OE-S), which is a giant expanding supershell thought to be created by the stellar winds and supernova explosions associated with the young, high mass stars of the Orion OB1 association. Based on *IRAS* dust emission measurements, the OE-S possesses an HI shell

mass of  $\sim 2.3 \times 10^5 M_\odot$  and a kinetic energy of  $3.7 \times 10^{51}$  erg (Brown et al. 1995). The kinematics of the Orion-Eridanus region is complex, with both large-scale motions and many smaller-scale variations present for both the ionized and neutral interstellar gas (Heiles et al. 1999). The entire OE-S region appears visually as a  $25^\circ$  diameter area of fragmented arcs of H- $\alpha$  emitting filamentary nebulosity (centered at  $\sim l = 190^\circ, b = -45^\circ$ ) with an associated expansion velocity of  $\sim 20 \text{ km s}^{-1}$  for the ionized gas (Reynolds & Odgen 1979). Heiles (1999) notes that for galactic longitudes,  $l > 210^\circ$ , the HI (neutral) gas is detected mostly at positive velocities whereas the H- $\alpha$  emitting gas resides at negative velocities, suggesting that the ionized gas may be confined to the near OE-S wall and the cold HI to its rear wall. For galactic longitudes,  $l > 210^\circ$ , the velocity structure is far more complex and the two component velocity structure becomes highly patchy. The energy source that created the OE-S is generally agreed to be the Orion OB1 complex, which is located some  $20^\circ$  below the galactic plane away from the OE-S. Recent distance determinations to Orion OB1

<sup>★</sup> Table 2 is only available in electronic form at <http://www.edpsciences.org>

by de Zeeuw (1999) have revealed that this stellar association is divided into 4 sub-groups, the closest being at a distance of only 336 pc.

The interior of this giant evacuated interstellar cavity contains hot ( $T \sim 2$  million K), low density ionized gas which emits strongly in the soft X-ray regime (Snowden et al. 1995). The morphology of this X-ray emission has been comprehensively studied by Burrows et al. (1993) who have discovered two distinct and independent emitting X-ray features (named the Eridanus X-ray enhancements, EXE1 and EXE2) that have been associated with different velocity components of the expanding ambient neutral HI gas. The HI filaments bounding the EXE1 feature move at negative velocities, with the largest extent of the low density cavity that contains the hot X-ray emitting gas appearing between  $-15$  and  $-5 \text{ km s}^{-1}$ . Although these data indicate that the near-side approaching neutral gas wall of the superbubble seems to provide a boundary to the low-density OE-S cavity, no similar structure has been identified at greater distances such that the hot interior gas is apparently free to escape into the lower galactic halo from the rear side of the superbubble.

The distance to the near-side of the OE-S cavity has been estimated by Guo et al. (1995) to be  $159 \pm 16$  pc. This determination was mainly based on the detection of an interstellar cloud component with an anomalous velocity of  $V_{\text{lsr}} = -19 \text{ km s}^{-1}$  seen in the NaI absorption spectrum towards the star BD  $-11$  702 (HD 22558). This star is of spectral type F5/6V (which is not ideally suited for interstellar absorption studies since narrow stellar lines can often confuse the recorded spectrum) and its distance was determined via spectro-photometric means since no Hipparcos satellite distance determination is currently available. Guo et al. also reported the detection of NaI absorption components at average velocities of  $V_{\text{lsr}} = -36.5$  and  $-21.8 \text{ km s}^{-1}$  towards the star HD 23393 ( $l = 201.2^\circ$ ,  $b = -46.8^\circ$ ,  $d = 234$  pc). At this distance from the Sun the Orion-Eridanus cavity should be one of the closest interstellar cavities that may abutt our own Local Bubble cavity and thus it should be visible as a large region of low neutral gas density in the 3-D NaI density maps of Lallement et al. (2003). Although the sampling of NaI absorption targets in the O-ES direction is not optimal for distances  $>200$  pc, there appears to be no sign of any large low neutral density cavity in Fig. 6 ( $l = 195^\circ$ – $15^\circ$  vertical plane cut) of Lallement et al. (2003) at the  $\sim 160$  pc distance inferred by Guo et al. (1995). Since any determination of the size and pressure of interstellar gas associated with the OES is dependent on its assumed distance, we decided to make a more complete sampling of the characteristics of neutral and partially ionized interstellar gas in this direction to a distance of  $\sim 500$  pc in order to map the extent of the possible shell-boundary to the OES.

In this Paper we present medium resolution ( $R \sim 7.5 \text{ km s}^{-1}$ ) absorption spectra of the interstellar NaI and CaII lines observed towards 16 early-type stars with distances ranging from 160 pc to  $>1$  kpc that lie in the general direction of the OES. These data are supplemented by high resolution NaI absorption measurements towards a further 13 stars that have been taken from the published literature. From these data we derive the kinematics, spatial extent and distances of

the various neutral and partially ionized absorption features detected towards this disturbed region of the ISM.

## 2. Observations

We have made interstellar NaI and CaII absorption observations towards the 16 early-type stars with identifier #'s 1–16 in Table 1, which lists the values of their galactic coordinates, visual magnitudes, spectral types, reddening and distance. We also list their measured values of equivalent width ( $EW$ ) for the NaI D2 and D1 absorption lines, in addition to that of the CaII K-line (in  $\text{m}\text{\AA}$ ). These data have been supplemented by a further 6 stellar targets (with identifier #'s 17–22) that have been observed with a similar spectral resolution at NaI by Genova & Beckman (2003), and by an additional 7 targets ( #'s 23–29) similarly observed at NaI by Penprase (1993). We have not included the NaI observations of 5 stars towards the high latitude cloud of Lynds 1569 by Penprase et al. (1990), since this narrow sight-line samples atypical interstellar gas contained within the core of a dense molecular cloud. The relevant astronomical data and equivalent width measurements for the additional stars we have decided to include are also listed in Table 1. Distances to all the targets have been taken from observations by the Hipparcos satellite (ESA 1997), and reddening values have mainly been taken from Tobin (1985), Savage et al. (1985), or calculated from values of  $(B-V)$  given in the Simbad on-line data-base. The positions of all 29 targets with respect to the optical  $H\alpha$  emission contours of the OE-S (as recorded by Boumis et al. 2001) are shown in Fig. 1. This figure clearly shows the familiar “hook” shaped  $H\alpha$  feature that supposedly defines the main emission cavity of the OE-S. On closer inspection, this feature appears to be composed of two spatially independent arcs of  $H\alpha$  emission which (following the work of Boumis et al.) shall be referred to as Arc A (the stronger emission feature at less negative galactic latitudes) and Arc B (the shorter arc on the right-hand side of the hook). Superposed on this figure are the approximate *ROSAT* contours of 0.75 keV X-ray emission, which in Fig. 1 are seen to be mostly located as a semi-circle of emission within Arc B. The reader is also referred to Fig. 6 of this paper (discussed later) in which the positions of Arcs A and B are plotted with respect to the radio 21 cm contours of gas with a velocity of  $+18$  to  $21 \text{ km s}^{-1}$  (as shown in Fig. 1 of Reynolds & Ogden 1979).

Both interstellar NaI D1 and D2 absorption lines at  $\sim 5890 \text{ \AA}$  and the CaII K-line at  $3933 \text{ \AA}$  were simultaneously obtained for our 16 targets during the nights of November 11–15th, 2003 using the GIRAFFE fiber-fed echelle spectrograph at the 1.9 m Radcliffe telescope of the South African Astronomical Observatory in Sutherland (RSA). The data were recorded using a Tektronix  $1024 \times 1024$  CCD detector and the spectra were extracted and calibrated using on-line procedures developed by Dr. Luis Balona (see <http://www.sao.ac.za/facilities/giraffe/index>). These software routines perform background subtraction, flat-fielding, optimal spectral order extraction and wavelength calibration using Th-Ar lamp spectra. The resolution of the resultant spectra was  $7.5 \text{ km s}^{-1}$  ( $R \sim 40000$ ) and the wavelength accuracy of the calibrated data

**Table 1.** Stellar target information.

ID #	Star	( <i>l</i> , <i>b</i> )	<i>m<sub>v</sub></i>	Sp	<i>E</i> ( <i>B</i> − <i>V</i> )	distance (pc)	<i>EW</i> (D2) mÅ	<i>EW</i> (D1) mÅ	<i>EW</i> (CaII) mÅ
1	HD 20001	(209.2°, −57.3°)	7.0	B3V	N/A	>1 kpc	102	51	151
2	HD 20319	(187.9°, −49.6°)	6.2	B9V	0.08	189(+45, −32)	113	96	52
3	HD 20340	(203.4°, −55.1°)	7.9	B3V	0.07	385(+214, −102)	110	71	49
4	HD 25558	(185.3°, −33.3°)	5.3	B3V	0.11	321(+142, −76)	176	156	103
5	HD 25631	(214.6°, −45.7°)	6.5	B3V	0.03	293(+92, −56)	171	98	72
6	HD 26739	(193.5°, −35.1°)	6.4	B5IV	0.03	429(+275, −120)	156	116	81
7	HD 26994	(211.1°, −41.8°)	6.9	B7III	0.04	375(+177, −92)	168	145	101
8	HD 27563	(201.5°, −36.8°)	5.8	B5III	0.02	232(+50, −34)	95	72	45
9	HD 28497	(208.8°, −37.4°)	5.6	B2V	0.10	483(+317, −137)	110	68	55
10	HD 29227	(199.5°, −31.6°)	6.3	B7III	0.04	268(+84, −52)	96	65	95
11	HD 29248	(199.3°, −31.4°)	3.9	B2III	0.02	180(+33, −25)	92	77	24
12	HD 29376	(189.3°, −25.3°)	7.0	B3V	0.14	676(+1365, −272)	254	186	104
13	HD 30076	(205.7°, −32.1°)	5.8	B2V	0.13	412(+210, −104)	224	153	88
14	HD 30211	(200.5°, −29.3°)	4.0	B5IV	0.01	163(+33, −25)	72	60	33
15	HD 31726	(213.5°, −31.5°)	6.1	B2V	0.05	305(+87, −55)	160	92	71
16	HD 32249	(206.6°, −27.7°)	4.8	B3VI	0.04	293(+93, −57)	120	75	64
17	HD 22920	(192.1°, −44.2°)	5.5	B9III	0.06	227(+46, −33)	135	82	–
18	HD 23363	(188.3°, −41.1°)	5.3	B7V	0.03	200(+35, −25)	326	210	–
19	HD 23466	(181.3°, −36.4°)	5.4	B3V	0.09	181(+30, −23)	185	132	–
20	HD 24263	(182.1°, −34.9°)	5.7	B5V	0.1	216(+102, −53)	212	146	–
21	HD 24388	(194.5°, −41.7°)	5.5	B8V	0.02	154(+25, −19)	39	20	–
22	HD 31512	(203.9°, −27.9°)	5.5	B6V	0.01	227(+93, −52)	82	66	–
23	HD 18873	(180.8°, −50.5°)	8.9	A5	0.11	326(+521, −125)	340	–	–
24	HD 19846	(171.9°, −41.1°)	8.6	B9	0.07	274(+114, −63)	268	–	–
25	HD 20404	(184.9°, −48.0°)	7.7	B8	0.07	218(+58, −38)	240	–	–
26	HD 24819	(191.1°, −38.8°)	8.1	A2	0.16	262(+141, −67)	165	–	–
27	HD 28856	(209.8°, −36.9°)	9.3	A1V	N/A	452(+830, −177)	147	–	–
28	HD 29851	(209.7°, −34.4°)	6.7	A2IV	0.1	161(+24, −19)	65	–	–
29	HD 32192	(208.6°, −28.7°)	7.7	B9	0.04	266(+112, −61)	89	–	–

was  $\sim\pm 0.05$  Å. All the spectra were well-exposed with typical S/N ratios in excess of 25:1 (slightly less for the CaII data) and all velocities subsequently reported in this paper are in the local standard of rest (lsr) frame of reference. The effects of contamination of the Na D-line profiles by narrow telluric water vapor features were removed by use of division by an absorption spectrum of a bright and nearby B star ( $\alpha$  Eri).

### 3. Interstellar analysis

We have determined the local stellar continua for all of the interstellar NaI and CaII absorption lines detected towards our 16 targets using a multi-order polynomial in order to produce the resultant residual intensity profiles shown in Figs. 2–5. These profiles were then fit with multiple absorption components (identified with interstellar gas “clouds”) using a line-fitting program described in Sfeir et al. (1999). This program assigns a 3-parameter theoretical fit to the observed absorption profiles by assigning values for the interstellar gas cloud component velocity, *V*, a Gaussian velocity dispersion, *b* and

a cloud component column density, *N*. This fitting procedure works very well for absorption components that are not saturated, but the process leads to large uncertainties in the derived column densities for the central cores of spectral lines that possess very high values of saturation. Fortunately, none of our sight-lines suffer from severe component saturation and hence the majority of the best-fit values of *b* and *N* shown in Table 2 for the absorption components detected in both the NaI and CaII lines are fairly well-constrained.

Consistent with the medium-resolution sampling of the data, our profile fits have been performed using the *minimum* number of absorption components. We have used the criterion of Vallerga et al. (1993) such that the addition of extra absorption components (which will always improve the fit at some level) is only justified if it results in a reduction of >1% of the chi-squared residual error between the observed and computed data points. We have also restricted the range of gas temperatures (and hence the derived *b*-value) in these fits to <20 000 K, in order to better match the expected physical conditions in these diffuse interstellar clouds. Errors for the derived

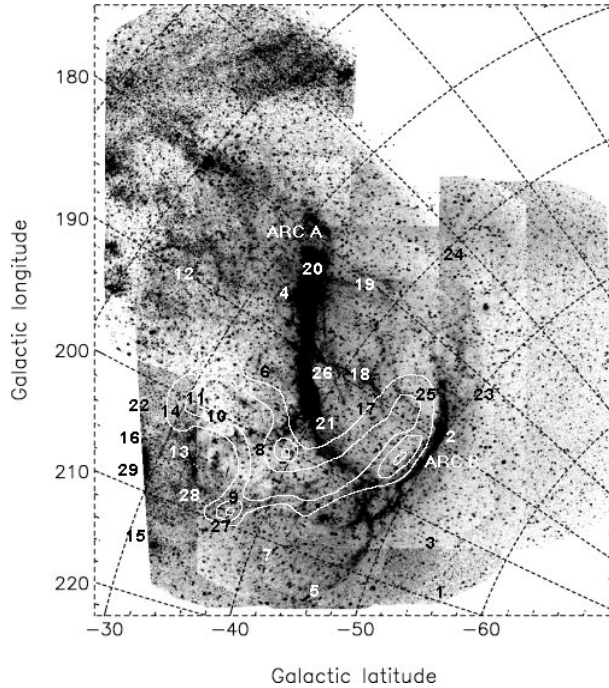


**Fig. 1.** Positions of the 29 target stars with respect to the optical H-alpha emission map of Boumis et al. (2001). Note the prominent central “hook-shaped” feature that is in fact comprised of 2 emission arcs. Targets numbered 1–16 are our presently observed stars, those numbered 17–22 have been observed by Genova & Beckman (2003) and targets numbered 23–29 have been observed by Penprase (1993). Superposed are the *ROSAT* 0.75 keV emission contours (white line) and the contour within which sight-lines exhibit an absorption component at  $V = -8.0 \text{ km s}^{-1}$  (dashed black line) that can be identified with an expanding shell of OE-S neutral gas with a distance of  $\sim 160 \text{ pc}$ .

component column densities (for unsaturated components) are also listed in Table 2. All of these model fits are shown superposed on their observed profiles in Figs. 2–5. In Table 2 we also list the model fits for the 6 stars observed at NaI by Genova & Beckman (2003) and for the 7 stars observed by Penprase (1993) and Penprase et al. (1990).

It should be noted that due to the medium-resolution of our data (i.e.  $\sim 7.5 \text{ km s}^{-1}$ ), the profiles in Figs. 2–5 likely contain many unresolved and blended absorption components and thus they do not reveal *all* of the underlying velocity structure along each sight-line. This is best illustrated by our observations towards the star HD 28497, which have presently revealed 6 cloud components in the NaI D-lines and 3 components in the CaII line. This can be compared with the observations of this same sight-line with the ultra-high resolving power of  $0.32 \text{ km s}^{-1}$  by Blades et al. (1995) who detected 13 absorption components in NaI and 10 components in CaII. We note, however, that our lower resolution data reveals all of the major (i.e. highest column density) absorption components along this sight-line and with very similar cloud velocities to those obtained by the ultra-high resolution observations. Therefore, we are confident that our present observations are able to reveal the presence and gross velocity structure of any dense (and neutral) gas that may be due to the interaction between the expansion of the OES and the ambient ISM.

## 4. Discussion

### 4.1. Absorption overview

Inspection of Table 2 and Figs. 2–5 reveal several aspects common to the absorption structure of the neutral ISM in this general galactic direction. For most of our observed sight-lines the majority of the cold and neutral NaI absorbing gas is formed over the restricted velocity range of  $-10$  to  $+15 \text{ km s}^{-1}$ . However, we note the exceptions of the sight-lines towards HD 20404 (#25), HD 28497 (#9), HD 30076 (#13) and HD 31726 (#15) which all have significant amounts of NaI absorption at velocities  $< -20 \text{ km s}^{-1}$ . Although the bulk of the CaII-line absorption (which samples neutral and partially ionized regions) also lies in the  $-10$  to  $+15 \text{ km s}^{-1}$  velocity range, these profiles are generally more complex than their NaI counterparts, with the CaII absorbing gas often being distributed within several velocity components. In two extreme cases (that of HD 28497 and HD 30076) the highest CaII column density components are detected at velocities  $< -30 \text{ km s}^{-1}$ .

We now use the data contained in Table 2 to identify absorption features that possess a common velocity in their NaI and CaII absorption spectra and to determine the approximate spatial extent of these absorption components with respect to the H- $\alpha$  and X-ray emission contours shown in Fig. 1.

### 4.2. The $V \sim +7.0 \text{ km s}^{-1}$ component: distance and spatial extent

Within the velocity interval of  $-10$  to  $+15 \text{ km s}^{-1}$  a strong absorption component is detected within  $\pm 3 \text{ km s}^{-1}$  of  $V_{\text{lsr}} = +7.0 \text{ km s}^{-1}$  in the NaI spectra of 21 of the 29 target stars. In 17 of these cases this is the main absorption component detected along that sight-line (i.e. the one with the largest NaI column density). This absorption component is also detected at a velocity close to  $V_{\text{lsr}} = +7.0 \text{ km s}^{-1}$  towards 12 of the 16 stars presently observed in the CaII K-line. We note that no detectable NaI absorption components have been reported by Lallement et al. (2003) for observations towards the stars HD 28763 ( $d = 123 \text{ pc}$ ), HD 21790 ( $d = 117 \text{ pc}$ ), HD 24587 ( $d = 118 \text{ pc}$ ), and HD 34968 ( $d = 140 \text{ pc}$ ) that all lie in the general direction of the OE-S. However, NaI is presently detected towards HD 30211 ( $d = 163 \text{ pc}$ ), HD 24388 ( $d = 154 \text{ pc}$ ) and HD 29851 ( $d = 161 \text{ pc}$ ). Therefore, we can confidently place a distance limit of  $140$ – $150 \text{ pc}$  for the cold and neutral NaI gas in this direction. This gas is characterized by a velocity of  $V \sim +7 \text{ km s}^{-1}$  and can be associated with the neutral gas boundary to the Local Bubble cavity, which has been placed at a distance of  $\sim 120$ – $150 \text{ pc}$  in this galactic direction by Lallement et al. (2003).

Gas with a velocity of  $V \sim +7.0 \text{ km s}^{-1}$  also corresponds to that of the main HI component revealed by 21 cm radio mapping of this area by Guo et al. (1995). The absence of gas with this velocity in 6 of our presently sampled sight-lines (i.e. #'s 6, 12, 15, 27 and 28) can be explained by the known patchy nature of the foreground neutral boundary to the Local Bubble that contains many gaps and interstellar tunnels that link it to other adjacent interstellar cavities. We note that all these 6 sight-lines

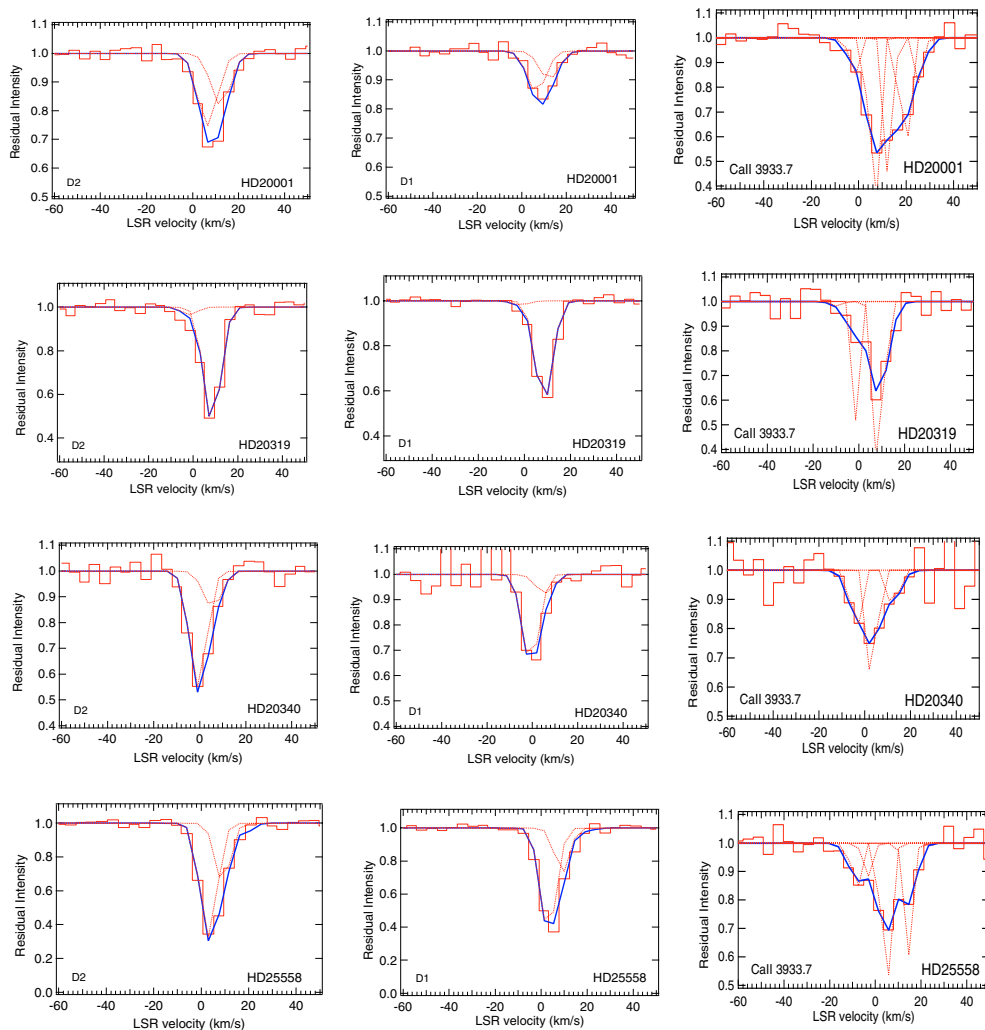


**Fig. 2.** Observed data and best-fit models for the interstellar NaI D2, D1 and CaII-K absorption lines recorded towards targets HD 20001(#1), HD 20319(#2), HD 20340(#3) and HD 25558(#4). Superposed on the residual intensity data points (light full line) are the multi-component best-fit absorption models (dark full line). The dotted lines indicate each of the components used in the model fits.

are located to the left of Arc A in Fig. 1, beyond the nominal contour of the  $V \sim -8 \text{ km s}^{-1}$  component shown in this figure.

#### 4.3. The $V \sim -8.0 \text{ km s}^{-1}$ component: distance and spatial extent

We have also detected a common (resolved) absorption component within  $\pm 3 \text{ km s}^{-1}$  of  $V_{\text{lsr}} \sim -8.0 \text{ km s}^{-1}$  in either/or both of the NaI and CaII profiles towards 12 of the 29 target stars (i.e. #'s 2, 4, 6, 8, 10, 11, 12, 15, 16, 18, 22 and 26). Gas with this velocity is only detected towards targets with sight-line distances  $> 180 \text{ pc}$  (this upper limit being defined by the detection towards both HD 29248 and HD 20319). If we assume a distance of 163–180 pc (the lower limit based on the non-detection towards HD 30211) for the  $V \sim -8.0 \text{ km s}^{-1}$  absorbing gas, then we can construct the approximate spatial contour for sight-lines with gas absorption at this velocity as depicted in Fig. 1. This contour essentially envelopes most of the H- $\alpha$  emitting Arcs A and B and the majority of the region of soft X-ray emission enhancement.

We can now identify the  $V \sim -8.0 \text{ km s}^{-1}$  component with the approaching shell of the OE-S, based upon the following arguments. Firstly, our present distance determination of 163–180 pc is in excellent agreement with the distance of  $159 \pm 16 \text{ pc}$  for the approaching near-shell of the OE-S cavity derived by Guo et al. (1995). We also note that the velocity difference between the line-of-sight absorption (at  $V \sim +7 \text{ km s}^{-1}$ ) and the  $V \sim -8 \text{ km s}^{-1}$  component is  $15 \text{ km s}^{-1}$ , which is identical to the expansion velocity of the H- $\alpha$  gas observed by Reynolds & Ogden (1979). In addition, Burrows et al. (1993) have shown that the HI filaments bounding the EXE1 feature are moving at negative velocities, with the largest extent of the low density cavity that contains the hot X-ray emitting gas appearing between  $-5$  and  $-15 \text{ km s}^{-1}$ . All these data would seem to support the notion that the  $V \sim -8 \text{ km s}^{-1}$  absorption feature is in fact the approaching (mainly neutral) gas shell that (partially) surrounds the hot and ionized gas within the OE-S cavity. This distance estimate also allows for a  $\sim 30$ – $40 \text{ pc}$  gap between the neutral boundary to the LB (at  $V \sim +7 \text{ km s}^{-1}$ ) and the approaching shell of the expanding OE-S gas.

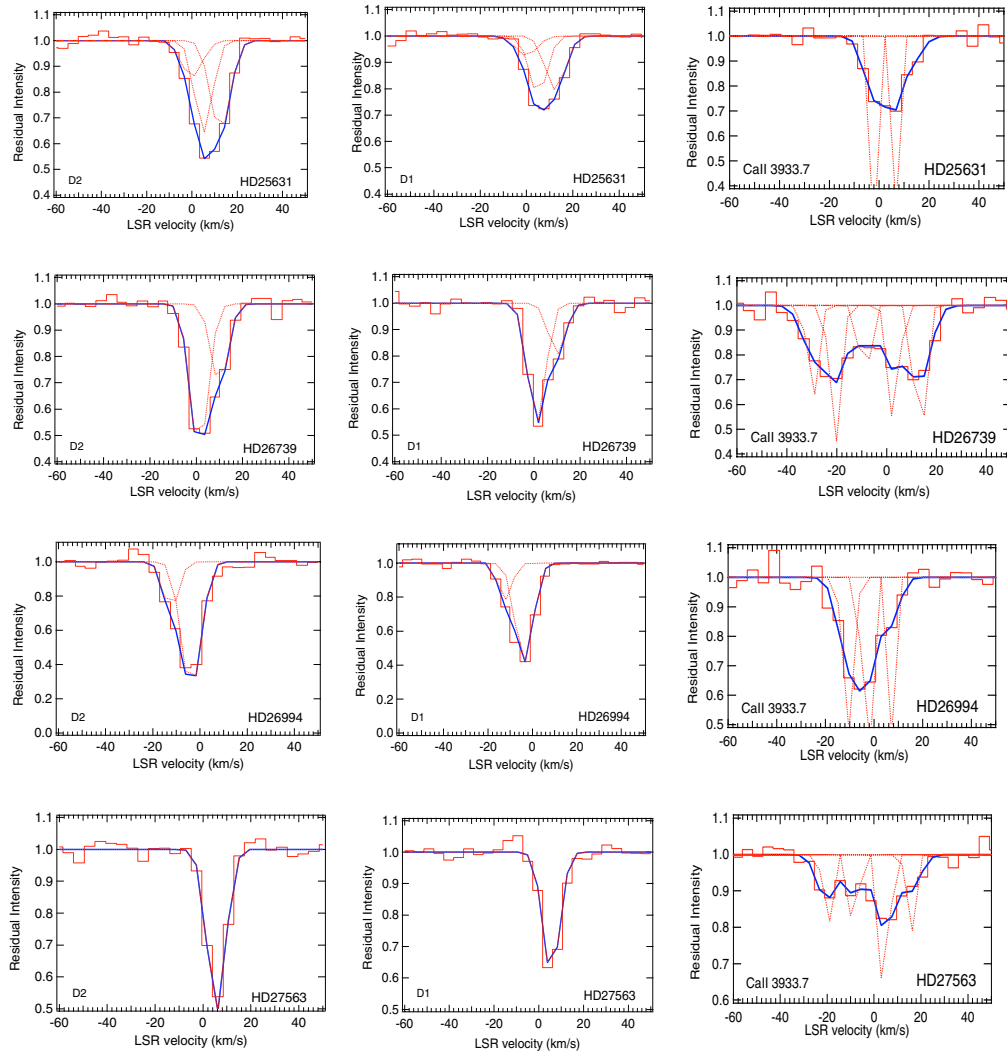


**Fig. 3.** Observed data and best-fit models for the interstellar NaI D2, D1 and CaII-K absorption lines recorded towards targets HD 25631(#5), HD 26739(#6), HD 26994(#7) and HD 27563(#8). Superposed on the residual intensity data points (light full line) are the multi-component best-fit absorption models (dark full line). The dotted lines indicate each of the components used in the model fits.

#### 4.4. Gas with negative velocities $< -15 \text{ km s}^{-1}$

NaI and/or CaII absorption components with more highly negative velocities in the range  $-15$  to  $-40 \text{ km s}^{-1}$  have been detected towards 8 targets. In 4 of these sight-lines (#6, 8, 10 and 27) we have detected a common velocity absorption component at  $V \sim -20 \text{ km s}^{-1}$ , and additionally in 4 of the sight-lines (#6, 9, #13 and #15) we detect gas with a common velocity of  $V \sim -28.5 \text{ km s}^{-1}$ . An additional absorption component at  $V \sim -33.5 \text{ km s}^{-1}$  is detected in just 3 sight-lines (#9, 13 and 25). For clarity, we have constructed just one contour in Fig. 6 (shown as the thick dark line) that delineates the area within which absorption components with velocities  $< -15 \text{ km s}^{-1}$  are detected. This contour has the approximate shape of an elongated ellipse and has a significant overlap with the area containing most of the soft X-ray emission contours shown in Fig. 1. Within these absorption contours, gas with a velocity of  $-15$  to  $-35 \text{ km s}^{-1}$  is only detected for sight-lines with distances  $> \sim 220 \text{ pc}$  (defined by the non-detection

towards # 17 and the detection towards # 25). Radio 21 cm HI observations towards the X-ray filament shadow regions of the OE-S by Guo et al. (1995) have revealed two main emission components with velocities of  $+8$  and  $-24 \text{ km s}^{-1}$ . The former (stronger) emission component has already been identified with the dense gas boundary to the Local Bubble, and the latter emission component can now be identified with a blend of gas clouds detected in absorption with velocities in the  $-20$  to  $-30 \text{ km s}^{-1}$  range.

#### 4.5. The $V \sim +13.4 \text{ km s}^{-1}$ component: distance and spatial extent

For gas with positive velocities  $> +10 \text{ km s}^{-1}$ , an absorption component with an average velocity of  $V \sim +13.4 \text{ km s}^{-1}$  is detected towards 12 of the 29 target stars (i.e. #'s 1, 3, 4, 5, 6, 8, 9, 10, 18, 23, 24 and 25). The non-detection of this velocity component towards HD 20319 (#2) and its detection along the angularly close sight-line to HD 23363 (#18) provides a

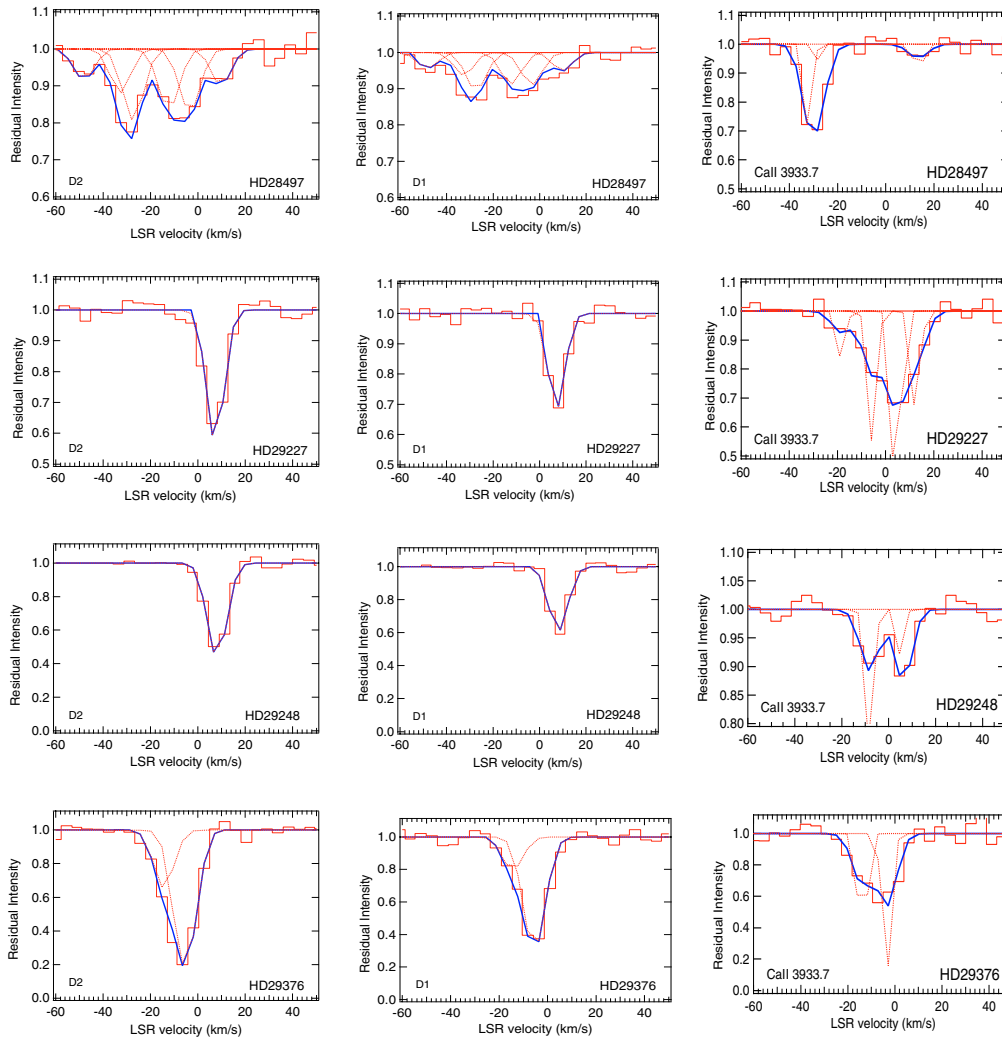


**Fig. 4.** Observed data and best-fit models for the interstellar NaI D2, D1 and CaII-K absorption lines recorded towards targets HD 28497(#9), HD 29227(#10), HD 29248(#11) and HD 29376(#12). Superposed on the residual intensity data points (light full line) are the multi-component best-fit absorption models (dark full line). The dotted lines indicate each of the components used in the model fits.

distance estimate of  $\sim 195$  pc for this component. In Fig. 6 (dotted line) we have drawn the approximate contours of the spatial extent of absorption for this velocity component, showing it to approximately mimic the “hook” shape of all Arc B and some of Arc A. We also note the similarity in the presently derived distance for this absorption component to that of the  $V \sim -8$  km s $^{-1}$  absorption component discussed previously.

Our observations confirm the general absence of gas with a velocity  $> +15$  km s $^{-1}$  throughout the whole of this region, thus supporting the notion that the OE-S may not possess a (coherently structured) expanding rear shell of neutral gas that could act as a vent into the overlying inner halo region for the expanding hot cavity gas. If such a large, receding (partial) shell does exist with a velocity  $> +15$  km s $^{-1}$  then our present observations place a distance limit of  $> 500$  pc for this gas. Gas absorption with a velocity  $\gg +15$  km s $^{-1}$  is only detected along one sight-line, towards HD 20001 (#1), which at a distance of  $> 1$  kpc is the most distant of all the 29 observed targets.

#### 4.6. The NaI/CaII ratios

The column density ratio of  $N(\text{NaI})/N(\text{CaII})$  is a widely used diagnostic of the physical conditions in neutral and partially ionized interstellar gas clouds and thus it is of interest to determine if its value is markedly different for the observed range of gas components. Values are listed in Table 2 for the cases where both a NaI and CaII cloud component has been identified with a similar velocity. For the 30 cases in which a component has been observed in *both* absorption lines, we determine a range of  $N(\text{NaI})/N(\text{CaII})$  ratios that range from 0.15 to 9.6 (we have omitted the case of HD 25558 since it possesses a highly saturated line-component). These ratios are typical for the diffuse, cold and neutral gas clouds that have been found throughout the ISM. The lowest values of the  $N(\text{NaI})/N(\text{CaII})$  ratio in the ISM tend to be found in absorption components with the highest negative velocities. We note that low values of this interstellar ratio are normally associated with the effects of increasing cloud velocity (Siluk & Silk 1974). In the extreme case of very

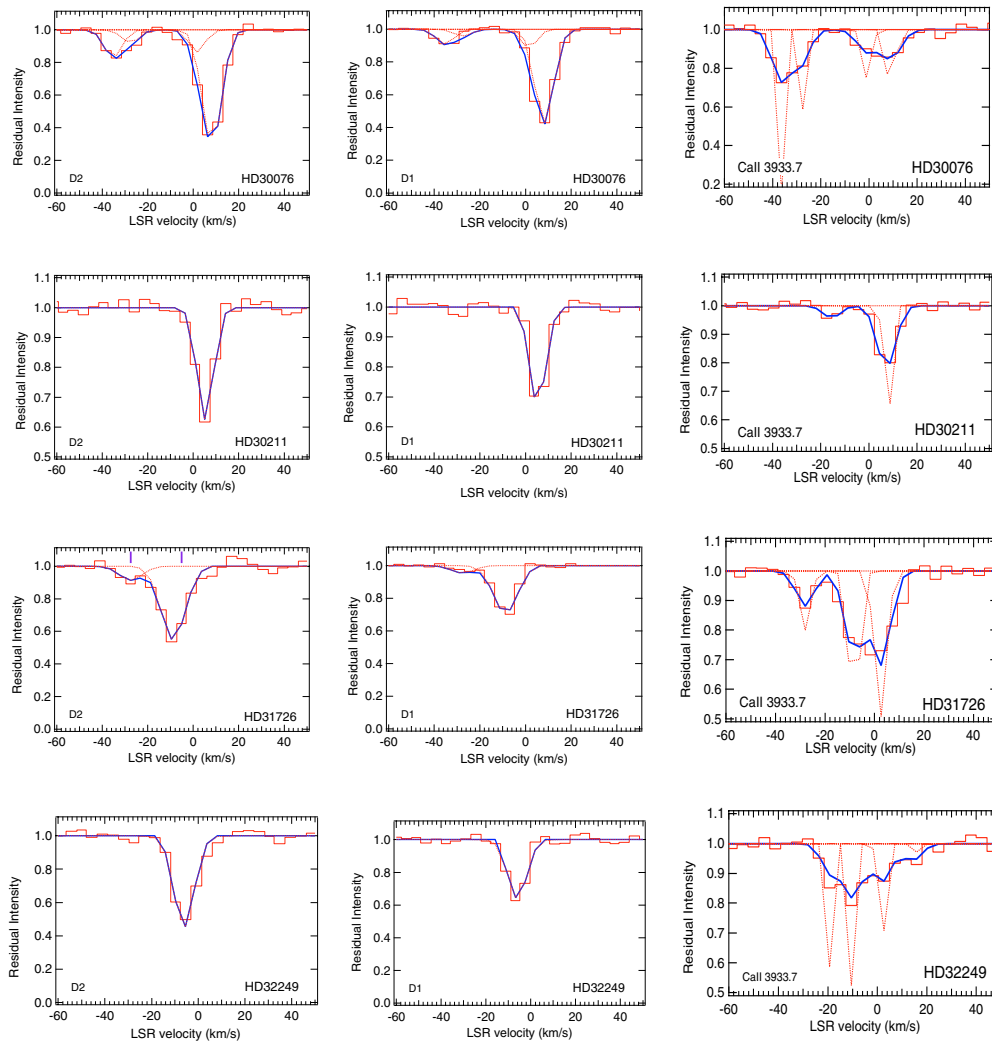


**Fig. 5.** Observed data and best-fit models for the interstellar NaI D2, D1 and CaII-K absorption lines recorded towards targets HD 30076(#13), HD 30211(#14), HD 31726(#15) and HD 32249(#16). Superposed on the residual intensity data points (light full line) are the multi-component best-fit absorption models (dark full line). The dotted lines indicate each of the components used in the model fits.

high cloud velocities ( $V > 30 \text{ km s}^{-1}$ ) interstellar shocks can be formed which cause the sputtering of interstellar grains which returns Ca back into the gas phase, thus producing an observed low value of the  $N(\text{NaI})/N(\text{CaII})$  ratio. We note that the values of the  $N(\text{NaI})/N(\text{CaII})$  ratio for both the  $V_{\text{lsr}} = -27.6$  and  $-33.5 \text{ km s}^{-1}$  components are all  $< 1.0$ , which would suggest that these clouds have been disrupted by a possible shock due to the expansion of the OE-S into the ambient ISM. As noted in the previous section, gas with velocities in this range is located in the same region as the soft X-ray emission contours, termed EXE1 by Burrows et al. (1993).

#### 4.7. Summary

The presently widely held picture of the OE-S cavity is derived from the pioneering work of Reynolds & Ogden (1979), in which both the famous Barnard's Loop and the Eridanus shell structures were thought to be created by one or more supernovae originating in the Orion OB association about  $2 \times 10^6$  years ago. The ionization state of the hot emitting gas

within this cavity is therefore being maintained by the action of the stellar winds/photo-ionization from the nearby OB stars. Comparisons between the X-ray and infrared data for the OE-S region by Burrows et al. (1993) and Snowden et al. (1995) have revealed an X-ray emitting structure that seemingly links the X-ray enhancement features in Eridanus to the Orion region. It has therefore been concluded that this cavity of hot and ionized gas is probably a giant stellar wind bubble, perhaps re-heated by a supernova explosion. Radio observations of this region by Brown et al. (1995) have revealed that the superbubble cavity itself is thought to be bounded by a large shell(s) of HI gas, centered approximately on ( $l = 200^\circ$ ,  $b = -33^\circ$ ). However, although this simple picture explains many observational aspects of the OE-S, both the distance and physical relationship of the H- $\alpha$  emitting Arc A (whose curvature is in the opposite sense to what one may expect from the simple superbubble model) to the adjacent Arc B is unclear.

Recent H- $\alpha$  observations of the OE-S by Boumis et al. (2001) have placed Arc A at a distance  $> 530 \text{ pc}$ , which is seemingly incompatible with the previously accepted

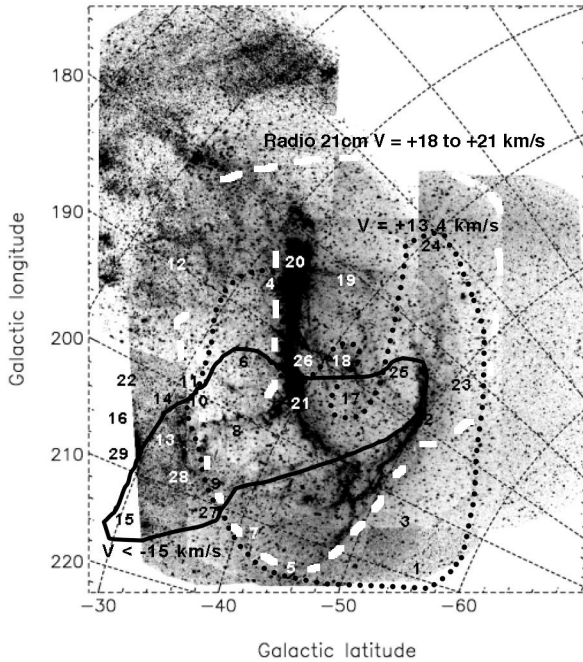


**Fig. 6.** Approximate spatial contours for sight-lines exhibiting absorption components at  $V = +13.4 \text{ km s}^{-1}$  and distances  $> 195 \text{ pc}$  (dotted black line) and  $V < -15 \text{ km s}^{-1}$  and distances  $> 220 \text{ pc}$  (thick black line) superposed on the  $H\alpha$  emission map of the OE-S by Boumis et al. (2001). Also shown is the approximate contours of the radio 21 cm emission (shown in thick white dashed lines) taken from Fig. 1 of Reynolds & Ogden (1979) for HI gas with a velocity in the range  $+18$  to  $+21 \text{ km s}^{-1}$ . Note how this spatially correlates with that of Arc A, but not Arc B. Targets numbered 1–29 are the same as in Fig. 1.

size and distance to the OE-S. In this new interpretation of the OE-S, the idea of a single superbubble cavity stretching from the Orion nebula to high galactic latitudes is discounted in favor of one in which several separate shells of HI gas are being driven by supernova explosions and/or stellar winds. In this case the  $H\alpha$  “hook” feature is in fact two separate and quite unrelated arcs of emitting gas with different distances, whose sight-line superposition merely gives the appearance of a single cavity-like structure to the OE-S. Our present detection of a multiplicity of absorption components with different positive and negative velocities (spanning the range  $-35$  to  $+25 \text{ km s}^{-1}$ ) and with different distances would seem to support such a scenario. Thus, the well-accepted notion that the OE-S has a single, well-defined neutral absorption boundary may be a misleading concept, since what we are most likely observing is a succession of fast-moving filamentary shells of approaching and receding gas.

Our simple maps of the spatial extent of the main absorption components observed towards the OE-S shown in Figs. 1 and 6, clearly show that the majority of the approaching and receding neutral gas is located in the area of the sky loosely bounded by  $(190^\circ < l < 210^\circ)$  and  $(-50^\circ < b < -30^\circ)$ . This is exactly the same region that contains the majority of the 0.75 keV X-ray emission observed by *ROSAT* (Snowden et al. 1995). Whereas the inner region bounded by the Arc B feature seems spatially well-correlated with those of *both* the X-ray emission and the approaching absorbing gas shells,

the Arc A feature does *not* share these attributes. Inspection of the Reynolds & Ogden (1979)  $H\alpha$  scans of this region clearly show that Arc A (positioned at  $\alpha = 4 \text{ h}$  in Fig. 1 of that paper) is nearly coincident with the center of a linear HI feature visible on Heiles (1976) map at a radial velocity of  $V_{\text{lsr}} \sim +20 \text{ km s}^{-1}$ . The approximate contour of this positive velocity radio emission is shown in our Fig. 6, which suggests a spatial correlation between this HI emission and that of  $H\alpha$  emission from Arc A. Our present absorption data have been unable to detect any gas with a velocity  $> +15 \text{ km s}^{-1}$  for distances  $< 500 \text{ pc}$ , which is in accord with the distance of  $> 530 \text{ pc}$  derived for Arc A by Boumis et al. (2001). Hence, Arc A and Arc B seem spatially unrelated and we confirm that the notion of the OE-S as a single superbubble cavity may be misleading. Thus, previous estimates forwarded by Guo et al. (1995) of the dynamic evolution of this superbubble feature based on simple models of the expansion of a SNR-driven or stellar-wind driven single-shell bubble (Mac Low & McCray 1988; Weaver et al. 1977) may be inappropriate. Ultraviolet absorption and emission observations of highly ionized species such as the OVI, NV, CIV and SiIV lines towards the “interaction” region mapped by the absorption contours of the negative velocity gas would provide important constraints on the physical nature of this highly disturbed medium and may help to establish the relationship between Arcs A and B, the OE-S cavity and the surrounding ISM.

## 5. Conclusion

We have obtained medium-resolution ( $7.5 \text{ km s}^{-1}$ ) spectra of the interstellar NaI and CaII absorption lines seen towards 16 early-type stars with distances ranging from 160–1 kpc in the general sight-line towards the Orion-Eridanus Superbubble (OE-S). We have fit the absorption components observed in the NaI and CaII lines with models of cloud-component velocity, doppler broadening and column density. These data have been supplemented by NaI data towards a further 13 sight-lines taken from the published literature. These measurements have revealed two main absorption components with velocities of  $V_{\text{lsr}} \sim +7.0$  and  $V_{\text{lsr}} \sim -8 \text{ km s}^{-1}$ . The former component is detected along  $\sim 70\%$  of the sight-lines and is associated with the neutral boundary to the Local Bubble cavity located at a distance of 140–150 pc. The absorption component at  $V \sim -8 \text{ km s}^{-1}$  is mainly detected towards a limited region of the sky bounded approximately by  $(190^\circ < l < 210^\circ)$  and  $(-50^\circ < b < -30^\circ)$ . If gas with this velocity is associated with an outer expansion shell of the OE-S then we can place its distance at 163–180 pc, in good agreement with previous distance estimates for the approaching neutral gas associated with the expansion of the OE-S. Three other absorption components with velocities of  $V_{\text{lsr}} = -20.4, -28.5$  and  $-33.5 \text{ km s}^{-1}$  have also been detected towards sight-lines that are spatially coincident with the contours of 0.75 keV X-ray emission recorded by *ROSAT*. Gas with such negative absorption velocities in the range  $-15$  to  $-35 \text{ km s}^{-1}$  is only detected towards sight-lines with distances  $> 220 \text{ pc}$ . A receding shell of gas with an absorption velocity of  $\sim +13.4 \text{ km s}^{-1}$  has been detected towards 12 targets with sight-line distances  $> 195 \text{ pc}$ . Our observations confirm the lack of gas with a velocity  $> +15 \text{ km s}^{-1}$

**Table 3.** Previously published NaI absorption line best-fit parameters.

ID #	Star	$V$ km s <sup>-1</sup>	$b$	$N$ (10 <sup>10</sup> cm <sup>-2</sup> )	Data source
17	<b>HD 22920</b>				
	...NaI...	+9.1	4.3	102 ± 20	Genova & Beckman (2003)
18	<b>HD 23363</b>				
	...NaI...	+12.8	2.9	47 ± 30	Genova & Beckman (2003)
		+7.4	3.7	130 ± 34	
		-5.0	3.2	49 ± 8	
		-10.2	13.2	33 ± 16	
19	<b>HD 23466</b>				
	...NaI...	+9.7	3.8	214 ± 5	Genova & Beckman (2003)
20	<b>HD 24263</b>				
	...NaI...	+9.2	4.8	219 ± 5	Genova & Beckman (2003)
21	<b>HD 24388</b>				
	...NaI...	+5.7	4.1	15 ± 9	Genova & Beckman (2003)
		-3.2	4.9	5 ± 1	
22	<b>HD 31512</b>				
	...NaI...	+10.0	3.6	42 ± 7	Genova & Beckman (2003)
		-7.6	7.5	7 ± 1	
23	<b>HD 18873</b>				
	...NaI...	+11.6	1.7	238	Penprase (1993)
		+8.4	5.5	190	
		+2.3	2.4	210	
24	<b>HD 19846</b>				
	...NaI...	+14.9	3.5	179	Penprase (1993)
		+8.8	3.2	>530	
		+1.0	4.2	31	
25	<b>HD 20404</b>				
	...NaI...	+13.9	2.2	18	Penprase (1993)
		+6.2	2.6	135	
		+0.6	1.8	32	
		-16.2	9.5	32	
		-33.7	7.1	24	
26	<b>HD 24819</b>				
	...NaI...	+8.6	3.0	243	Penprase (1993)
		-8.7	6.3	31	
27	<b>HD 28856</b>				
	...NaI...	+0.2	1.6	189	Penprase (1993)
		-10.6	2.7	14	
		-22.8	5.1	21	
28	<b>HD 29851</b>				
	...NaI...	+0.7	1.3	120	Penprase (1993)
29	<b>HD 32192</b>				
	...NaI...	-2.4	5.0	38	Penprase (1993)

throughout the entire region, suggesting that if an expanding rear shell to the OE-S exists, then its distance must be >500 pc.

Column density ratios of  $N(\text{NaI})/N(\text{CaII})$  for the most negative velocity components are <1.0, suggesting that this gas has been disrupted by a possible shock event associated with the expansion of the OE-S.

Our observations do not support the notion that the OE-S can be described by a single expanding shell of gas surrounding an elongated OE-S cavity, and instead a far more complex model that may involve multiple supernovae and/or stellar wind-driven shocks that produce separate shells of expanding

gas seems more appropriate. We have confirmed that the prominent H- $\alpha$  “hook” feature that dominates the appearance of the OE-S is in fact composed of two quite separate emission arcs. One of these features, Arc A, has a distance > 500 pc and thus may not be associated with the OE-S cavity. We suggest that future ultraviolet absorption studies of the region of the OE-S that contains the majority of negative velocity gas components may help in better understanding the physical state of any interaction between the expanding OE-S and the ambient ISM.

*Acknowledgements.* We are grateful to the staff and directorate of the South African Astronomical Observatory and wish to thank both

Dr. David Buckley and Francois van Wyk for their patience in training us as users of the excellent spectroscopic instrumentation at the Sutherland Observatory. B.Y.W. and S.S. acknowledge funding from the NASA *FUSE* project under contract NAS5-32985 to the Johns Hopkins University.

## References

- Blades, C., Sahu, M., He, L., et al. 1997, *ApJ*, 478, 648  
 Boumis, P., Dickinson, C., Meaburn, J., et al. 2002, *MNRAS*, 320, 61  
 Brown, A., Hartmann, D., & Burton, W. 1995, *A&A*, 300, 903  
 Burrows, D., Singh, K., Nousek, J., Garmire, G., & Good, J. 1993, *ApJ*, 406, 97  
 Cox, D., & Smith, B. 1974, *ApJ*, 189, L105  
 De Zeeuw, P., Hoogerwerf, R., de Bruijne, J., Brown, A., & Blaauw, A. 1999, *AJ*, 117, 354  
 ESA 1997, The Hipparcos Satellite Catalogue, ESA SP-1200  
 Genova, R., & Beckman, J. 2003, *ApJS*, 145, 355  
 Guo, Z., Burrows, D., Sanders, W., Snowden, S., & Penprase, B. 1995, *ApJ*, 453, 256  
 Heiles, C. 1976, *ApJ*, 208, L137  
 Heiles, C., Haffner, L., & Reynolds, R. 1999, *New Perspectives on the Interstellar Medium*, ed. A. R. Taylor, T. L. Landecker, & G. Joncas (San Francisco: ASP), ASP Conf. Ser., 168, 211  
 Lallement, R., Welsh, B. Y., Vergerly, J. L., Crifo, F., & Sfeir, D. 2003, *A&A*, 411, 447  
 Mac Low, M., & McCray, R. 1988, *ApJ*, 324, 776  
 Penprase, B. 1993, *ApJS*, 88, 433  
 Penprase, B., Blades, J. C., Danks, A., & Crane, P. 1990, *ApJ*, 365, 241  
 Reynolds, R., & Ogden, P. 1979, *ApJ*, 229, 942  
 Savage, B., Massa, D., Meade, M., & Wesselius, P. 1985, *ApJS*, 59, 397  
 Sfeir, D., Lallement, R., Crifo, F., & Welsh, B. Y. 1999, *A&A*, 346, 785  
 Siluk, R., & Silk, J. 1974, *ApJ*, 192, 51  
 Snowden, S., Burrows, D., Sanders, W., Aschenbach, B., & Pfeffermann, E. 1995, *ApJ*, 439, 399  
 Tobin, W. 1985, *A&A*, 142, 189  
 Vallerga, J., Vedder, P., Craig, N., & Welsh, B. Y. 1993, *ApJ*, 411, 729  
 Weaver, R., McCray, R., Castor, J., Shapiro, P., & Moore, R. 1977, *ApJ*, 218, 377  
 Welsh, B. Y., Sallmen, S., Sfeir, D., & Lallement, R. 2002, *A&A*, 391, 705

# Online Material

**Table 2.** NaI and CaII absorption line best-fit parameters.

ID #	Star	$V$ km s <sup>-1</sup>	$b$	$N$ (10 <sup>10</sup> cm <sup>-2</sup> )		$V$ km s <sup>-1</sup>	$b$	$N$ (10 <sup>10</sup> cm <sup>-2</sup> )	NaI/CaII
1	<b>HD 20001</b>				...CaII...	+26.0	2.3	13 ± 2	–
	...NaI...					+19.0	2.5	52 ± 10	–
		+12.2	3.2	22 ± 5		+12.8	2.3	54 ± 10	0.41
		+6.6	3.3	33 ± 6		+6.4	2.5	87 ± 8	0.38
						–2.4	2.5	13 ± 3	–
2	<b>HD 20319</b>				...CaII...	+8.6	2.7	85 ± 15	2.7
	...NaI...	+8.6	1.6	230 ± 30		–1.9	0.8	23 ± 5	0.15
		–1.6	1.0	3.5 ± 1					–
3	<b>HD 20340</b>				...CaII...	+12.7	2.2	14 ± 3	–
	...NaI...	+5.4	2.7	16 ± 3		+4.5	2.5	41 ± 8	0.39
		–1.0	1.5	125 ± 25		–3.0	2.5	22 ± 5	5.7
4	<b>HD 25558</b>				...CaII...	+14.4	2.5	33 ± 5	–
	...NaI...	+9.0	1.0	85 ± 15		+4.6	2.9	55 ± 6	13.6
		+3.1	1.6	750 ± 60		–3.4	2.8	10 ± 2	–
						–8.9	2.5	15 ± 3	–
5	<b>HD 25631</b>				...CaII...	+13.6	0.5	25 ± 5	2.0
	...NaI...	+12.5	3.5	50 ± 10		+5.6	1.1	100 ± 15	0.55
		+5.5	2.2	55 ± 15		–2.5	1.2	55 ± 10	0.33
		–1.0	4.3	18 ± 4					
6	<b>HD 26739</b>				...CaII...	+13.0	2.9	65 ± 10	0.77
	...NaI...	+11.0	1.5	50 ± 10		+2.5	2.9	50 ± 10	3.7
		+1.5	1.9	185 ± 20		–9.0	2.5	30 ± 10	–
						–20.5	2.9	60 ± 8	–
						–29.7	2.8	37 ± 5	–
7	<b>HD 26994</b>				...CaII...	+6.5	0.9	35 ± 5	–
	...NaI...	–3.8	3.1	205 ± 25		–3.1	2.0	85 ± 15	2.4
		–12.0	0.9	65 ± 15		–10.5	2.9	55 ± 10	1.2
8	<b>HD 27563</b>				...CaII...	+15.6	2.4	17 ± 4	–
	...NaI...	+5.6	1.8	130 ± 20		+4.5	2.5	38 ± 8	3.4
						–8.5	2.5	18 ± 4	–
						–20.4	1.8	21 ± 4	–
9	<b>HD 28497</b>				...CaII...	+13.4	2.5	7.8 ± 1	3.4
	...NaI...	+10.0	3.3	11 ± 3					–
		–3.4	3.7	21 ± 5					–
		–12.3	3.8	20 ± 5					–
		–27.4	3.6	25 ± 5		–27.0	0.7	25 ± 4	1.0
		–32.7	3.4	14 ± 4		–31.0	1.2	72 ± 10	0.2
10	<b>HD 29227</b>				...CaII...	+12.6	2.5	30 ± 6	–
	...NaI...	+7.0	1.6	97 ± 15		+5.0	2.5	70 ± 10	1.4
						–5.5	2.4	40 ± 7	–
						–18.0	2.5	12 ± 3	–
11	<b>HD 29248</b>				...CaII...	+6.5	1.1	23 ± 5	5.2
	...NaI...	+8.0	2.4	120 ± 15		–8.0	2.5	18 ± 4	–
12	<b>HD 29376</b>				...CaII...	–3.4	2.5	125 ± 15	2.8
	...NaI...	–5.0	3.3	350 ± 45		–13.8	2.4	72 ± 8	0.7
13	<b>HD 30076</b>				...CaII...	+9.0	2.5	26 ± 5	9.6
	...NaI...	+1.0	0.3	135 ± 15		–0.5	2.4	20 ± 4	6.8
		–27.5	2.1	8 ± 3		–28.5	1.0	40 ± 8	0.2
		–35.5	2.5	20 ± 5		–36.5	1.2	65 ± 10	0.3
14	<b>HD 30211</b>				...CaII...	+7.3	1.7	44 ± 6	4.8
	...NaI...	+5.5	1.0	210 ± 30		–15.4	0.5	8.0 ± 2	–
15	<b>HD 31726</b>				...CaII...	+2.5	3.2	58 ± 8	–
	...NaI...	–8.8	3.4	100 ± 10		–8.3	3.2	50 ± 6	2.0
		–27.5	2.7	12 ± 2		–28.0	3.1	18 ± 2	0.67
16	<b>HD 32249</b>				...CaII...	+7.6	6.3	29 ± 3	–
	...NaI...	–6.5	3.2	100 ± 15		–7.5	6.3	49 ± 5	2.0